Durable Ni_3N porous nanosheets array for non-noble metal methanol oxidation reaction

Cite as: APL Mater. 11, 051112 (2023); doi: 10.1063/5.0148124
Submitted: 28 February 2023 • Accepted: 18 April 2023 •
Published Online: 12 May 2023

Wanying Zhang,[1] Madiha Rafiq,[1] Jingcheng Lu,[1] Abebe Reda Woldu,[1] Jianhong Zhou,[1] Hong Xia,[1,2] Paul K. Chu,[3,a)] Liangsheng Hu,[1,2,a)] and Fushen Lu[1,2,a)]

AFFILIATIONS

[1] Department of Chemistry and Key Laboratory for Preparation and Application of Ordered Structural Materials of Guangdong Province, Shantou University, Shantou, Guangdong 515063, People's Republic of China
[2] Chemistry and Chemical Engineering Guangdong Laboratory, Shantou 515063, People's Republic of China
[3] Department of Physics, Department of Materials Science and Engineering, and Department of Biomedical Engineering, City University of Hong Kong, Tat Chee Avenue, Kowloon, Hong Kong, China

This paper is part of the Special Topic on Materials Challenges for Catalysis.
[a)] **Authors to whom correspondence should be addressed:** paul.chu@cityu.edu.hk; lshu@stu.edu.cn; and fslu@stu.edu.cn

ABSTRACT

Direct methanol fuel cells (DMFCs) are energy carriers with a significant high energy density, easy implementation, a low operating temperature, and a convenient methanol fuel storage, rendering them a reasonable alternative for portable applications. However, there are several substantial barriers to the widespread use of DMFCs that must be addressed. Noble metal-based catalysts have long been regarded as outstanding electrocatalysts for fuel cells, but their high cost and low durability have kept them from becoming widely used. Nickel-based electrocatalysts are possible replacements for expensive noble metal catalysts owing to their low price, high durability, and remarkable surface oxidation properties. Herein, we develop an incredibly active and remarkably stable electrocatalyst for the methanol oxidation reaction (MOR) via a simple hydrothermal method coupled with nitridation to prepare highly porous Ni_3N nanosheets arrays supported by nickel foam (NF) substrate. The *in situ* growth of highly porous nanosheets on NF (NSAs/NF) exposes more active sites and allows fast charge/mass transfer, creating synergistic effects between Ni_3N and NF. As a result, the strong interaction between Ni_3N and NF prevents leaching and renders the catalyst highly stable for over 20 h with a 72.58% retention rate, making it among the best retention rates reported recently for comparable Ni-based catalysts. Based on these findings, nickel nitride appears to be an excellent electrocatalyst for fuel cell applications.

INTRODUCTION

Methanol is one of the most interesting fuels due to its high energy density, portability, safety while handling, solubility in aqueous solutions, accessibility, and potential generation from renewable energies.[1–3] With the rising availability of methanol, the obstacle will be creating a reliable device to transform methanol into electricity. Direct-methanol fuel cells (DMFCs), which utilize methanol as a fuel and convert chemical energy into electrical energy by directly oxidizing with oxygen (O_2) from the air to carbon dioxide (CO_2) and water, have drawn considerable research interest owing to their easy mobility and energy density.[4] One of the key components of DMFCs is the electrocatalyst, which improves the methanol oxidation reaction (MOR) efficiency on the anode.[5] Sustainable energy storage and conversion is a key driver for the development of nanostructured electrocatalysts, but it is crucial to design catalysts with high activity and durability for MOR. Pt or Pt-based alloys have been reported to be the most active catalysts for some electrochemical reactions such as biosonsing,[6] hydrogen evolution reaction,[7,8] oxygen reduction reaction,[9] and

MOR, but CO poisoning and the high cost have limited their commercialization.[10] Therefore, Pt-free electrocatalysts with high activity, high reliability, and stability are required for practical applications and the market acceptance of DMFC technologies.

Among non-platinum metal catalysts, nickel-based catalysts are considered the most promising to replace Pt because of their low cost, resistance to poisoning, good surface oxidation properties, and high catalytic activity toward electro-oxidation of alcohols.[11] Among them, the Ni_3N catalyst has attracted considerable interest due to abundant active sites, rapid charge transfer rate, and notable catalytic performance.[12,13] Theoretical calculations predict that metal nitride electrocatalysts possess many advantages over pure metals.[14] Moreover, the presence of nitrogen strongly influences the electronic properties of the metal by increasing the density of electrons on the surface. However, Ni_3N is vulnerable to passivation under alkaline environments, and the activity and durability of Ni_3N catalysts in alkaline solutions are substantially lowered.[15] Previous research has exploited activated carbonaceous additives and metal foil/foam/mesh substrates as the catalyst support that enhanced the conductivity and stability of the electrode materials.[16,17]

Notably, catalysts with accessible active surface sites promote electrocatalytic activity in a single direction.[18] Nickel is also recognized as a outstanding flexible support, and researchers have used Ni foam as a substrate.[17] Also, Ni foam (NF) is extraordinarily stable in alkaline solutions and can be mass-produced with diverse surface and structural modifications. Herein, we design unique self-supported nanosheets of Ni_3N anchored on a 3D Ni foam skeleton by using a simple two-step method. This unique *in situ* growth of Ni_3N NSAs on Ni foam (Ni_3N NSAs/NF) is beneficial in many ways; for example, no additional binder or conducting agent is required to prepare the electrode, making handling very easy and cheap. With a large specific and electrochemically accessible surface area, Ni foam provides abundant catalytic active sites by dispersing the active centers, resulting in a high loading of Ni_3N NSAs. Last but not least, the stability of the catalyst improves due to the seamless contact between the nanosheet arrays of Ni_3N and Ni foam, ensuring tight integration that prevents leaching and triggers rapid charge transfer. Detailed catalytic tests show that the Ni_3N NSAs/NF not only has enhanced electrocatalytic properties in MOR but also has an improved stability for 20 h in methanol oxidation under alkaline conditions. The exceptional electrochemical activity of the Ni_3N NSAs/NF system originates from the high conductivity, exposed edges of Ni_3N nanosheets, and synergistic effects between Ni_3N NSAs and Ni foam.

EXPERIMENTAL SECTION

Synthesis of $Ni(OH)_2$ NSAs/NF

A simple hydrothermal technique is used to create the $Ni(OH)_2$ NSAs/NF hybrid structure. Typically, 26.25 mmol urea, 10.5 mmol NH_4F, and 3.93 mmol $Ni(NO_3)_2{\cdot}6H_2O$ were mixed in 70 mL H_2O and stirred at room temperature for 1 hour to ensure the homogenous mixing. The mixture was transferred to a 100 ml Teflon reactor. A piece of nickel foam (NF) with a size of 2 × 3 cm^2 was cleaned by soaking in 1M HCl for 30 min, washed with water, and placed vertically in the Teflon reactor containing the mixture. The reactor was put in an oven at 100 °C for 8 h to produce the $Ni(OH)_2$ nanosheet array precursor.

Synthesis of Ni_3N nanosheet arrays and control samples

The $Ni(OH)_2$ NSAs/NF hybrid was placed in a tube furnace and annealed at 350, 380, 400, 430, and 450 °C for 3 h under NH_3 (50 SCCM), respectively. After reacting for 3 h, the product was collected and denoted as Ni_3N–Y (Y = 350, 380, 400, 430, and 450). To compare, the control catalysts were synthesized using the same technique with slight changes. NF-400 was prepared by annealing the NF at 400 °C. The $Ni(OH)_2$ precursor was annealed at 400 °C for 3 h under air in a muffle furnace and under an Ar/H_2 (5 Vol % H_2) atmosphere in the tube furnace to obtain nickel oxide (NiO-400) and metal Ni (Ni-400) nanoparticles, respectively.

Material characterization

Transmission electron microscopy (TEM) was conducted on a Tecnai G2 F20. The specimens for TEM were prepared by depositing a drop of a dilute catalyst dispersion onto a mica substrate and a holey carbon-coated copper grid, respectively. X-ray diffraction (XRD) was carried out on a Bruker D8 advance x-ray diffractometer. Scanning electron microscopy (SEM) and EDS were performed on a Hitachi S4800 field-emission microscope. The surface compositions of catalysts were determined by x-ray photoelectron spectroscopy (XPS).

Electrochemical evaluation

All electrochemical tests were performed using a three-electrode electrochemical system with a prepared Ni_3N NSAs/NF (0.5 × 0.5 cm^2) as the working electrode, a saturated calomel electrode (SCE) as the reference electrode, and a Pt wire as the counter electrodeon on the CHI 760E electrochemical workstation. Cyclic voltammetry (CV), chronoamperometry (CA), electrochemical active surface area (ECSA), and electrochemical impedance spectroscopy (EIS) were carried out. All tests were conducted in a 1.0 M KOH solution bubbled with N_2 in the absence or presence of methanol.

RESULTS AND DISCUSSION

As shown in Scheme 1, the highly porous Ni_3N nanosheet arrays are fabricated by a facile two-step approach. Firstly, the $Ni(OH)_2$ NSAs are grown on well-cleaned, highly porous NF as a conductive template by a hydrothermal process. The $Ni(OH)_2$ NSAs/NF nitride is annealed at 400 °C under flowing NH_3 to obtain the Ni_3N NSAs/NF composite. The Ni_3N NSAs/NF electrode is evaluated for MOR. X-ray diffraction (XRD) is employed to study the crystal phases and structural components. Figure 1(a) displays the XRD patterns of the as-prepared $Ni(OH)_2$ and Ni_3N–Y (Y = 350, 380, 400, 430, and 450) NSAs/NF samples. By comparing the XRD patterns of Ni_3N NSAs/NF prepared at different temperatures, Ni_3N-380 and Ni_3N-400 NSAs/NF show the formation of Ni_3N, as the peaks at 38.6°, 42.1°, 44.5°, 58.5°, 70.6°, and 78.4° match the (110), (002), (111), (112), (300), and (113) crystal planes of the hexagonal Ni_3N (PDF#10-0280), respectively. A low temperature (350 °C) leads to partial $Ni(OH)_2$ un-transformation, while high temperatures (430 and 450 °C) reduce $Ni(OH)_2$ to metallic nickel. The morphology of the as-prepared samples is characterized

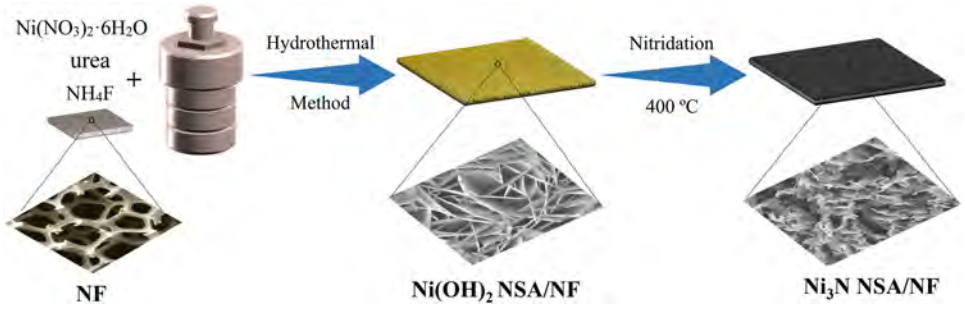

SCHEME 1. Schematic illustration of the fabrication of the Ni_3N NSAs/NF.

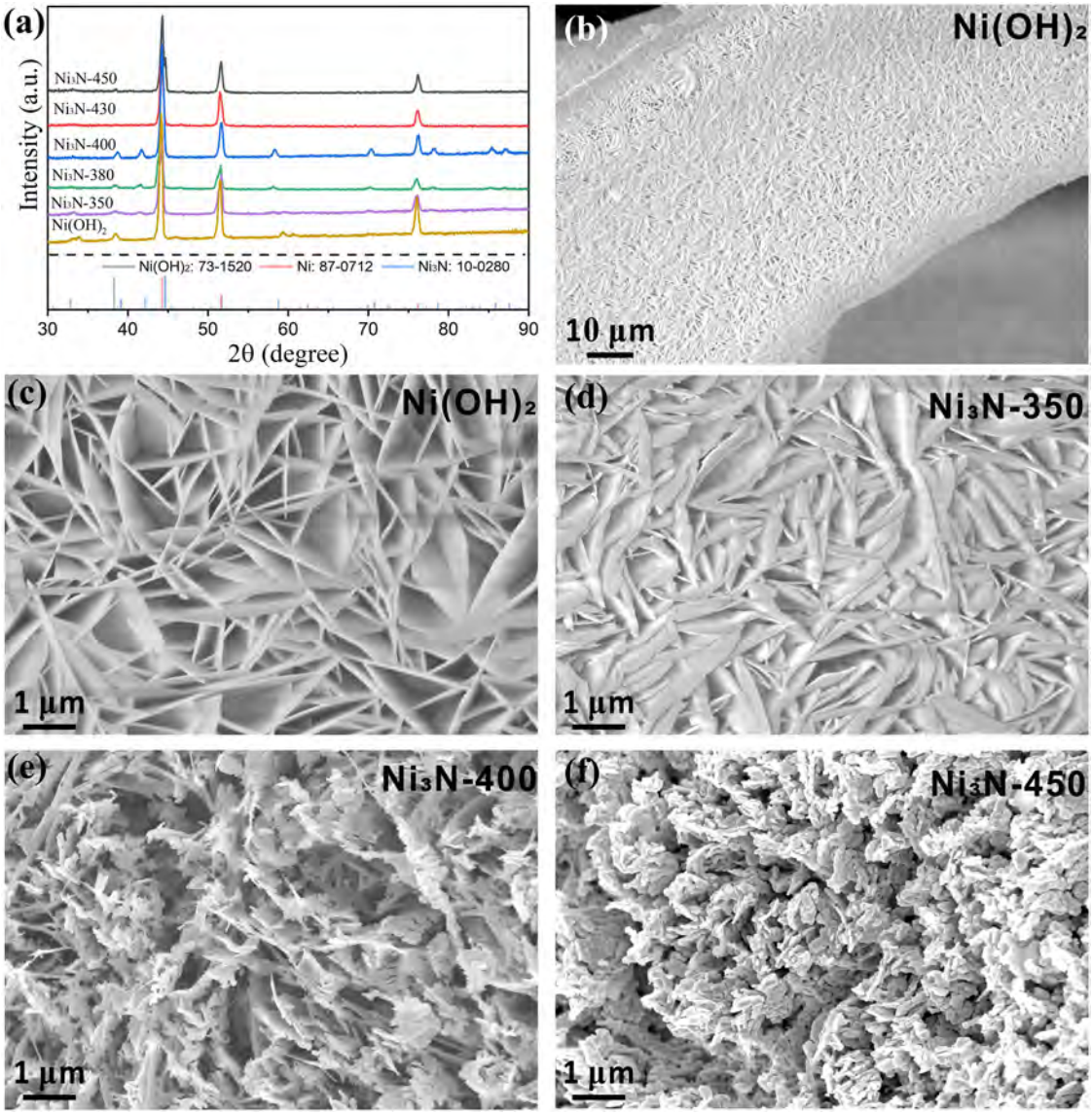

FIG. 1. (a) XRD spectra for Ni, $Ni(OH)_2$, and Ni_3N at different temperatures. SEM images of [(b) and (c)] $Ni(OH)_2$ precursors, (d) Ni_3N-350, (e) Ni_3N-400, and (f) Ni_3N-450.

by SEM and high resolution transmission electron microscopy (HR-TEM). As shown in Fig. 1(b), the surface of the pure NF is relatively rough after reacting with the nickel salt aqueous solution, revealing the successful preparation of $Ni(OH)_2$ nanosheet arrays. Figure 1(c) shows that the rough surface is mainly because of uniformly vertically aligned, interconnected nanosheets with large interlayer clearance on the nickel foam. As mentioned above, Ni_3N NSAs/NF is derived from the $Ni(OH)_2$ precursor through nitridation under NH_3, and different temperatures are adopted in the nitridation process to explore the best conditions. According to the SEM images [Figs. 1(d)–1(f)], the smooth nanosheet arrays of $Ni(OH)_2$ gradually change to scaly standing porous nanosheets on the nickel foam. As the temperature goes up, the surface of the nanosheets becomes rough and porous, mainly due to the gas release and dehydration of $Ni(OH)_2$ during the nitridation process.[19] As shown in Fig. 1(e), the SEM image of Ni_3N NSAs/NF-400 clearly shows the formation of highly porous nanosheets with the most suitable size and thickness, which is also in agreement with XRD. This unique porosity and rough surface produce numerous channels for rapid ion transport and provide large surface active sites for facilitating electrocatalysis. The elemental mapping results in Fig. S1 indicate that Ni and N are homogeneously distributed in Ni_3N NSAs/NF-400, revealing that the Ni_3N nanosheets have a uniform composition.

The TEM image [Fig. 2(a)] shows that the Ni_3N-400 nanosheet is composed of numerous small nanoparticles. The HR-TEM image of Ni_3N-400 in Fig. 2(b) reveals well-resolved lattice fringes with an interplanar d-spacing of 0.203 and 0.215 nm consistent with the (111) and (002) crystal planes of hexagonal Ni_3N. To identify the chemical state of the surface elements of the catalyst, x-ray photoelectron spectroscopy (XPS) is performed. As shown in Figs. 2(c) and 2(d), the peaks of Ni 2*p* [Fig. 2(c)] at 852.7, 855.8, and 873.5 eV arise from Ni-N, and the other peaks can be ascribed to Ni^{2+} from surface oxidized Ni species.[12] The satellite peak at 861.4 eV is attributed to the shake-up excitation of the high-spin nickel ions.[18] Figure 2(d) shows the XPS spectra of N 1*s* deconvoluted into three peaks positioned at 397.8, 399.3, and 403.1 eV, which are assigned to Ni-N in Ni_3N, absorbed N-H_x, and oxidized-N, respectively.[20] The intense peak at 397.8 eV confirms the formation of metal nitride by ammonolysis.[21]

The electrochemical properties of the as-prepared catalyst (Ni_3N-400) are investigated by CV, but before that, a contrast test is performed to evaluate the MOR characteristics. It has been shown that the oxygen evolution reaction (OER) and MOR may take place under identical potential ranges after the formation of NiOOH (Ni^{3+}) on the Ni-based catalysts in an alkaline solution.[22] Therefore, to determine the potential range of the catalyst, CV is conducted in 1.0M KOH with/without the methanol solution in the 1.1–1.8 V potential window. Figure 3(a) clearly shows the MOR characteristics of the Ni_3N-400 catalyst between 1.5 and 1.7 V after the oxidation peak of Ni^{2+} appears in the absence of the methanol solution,

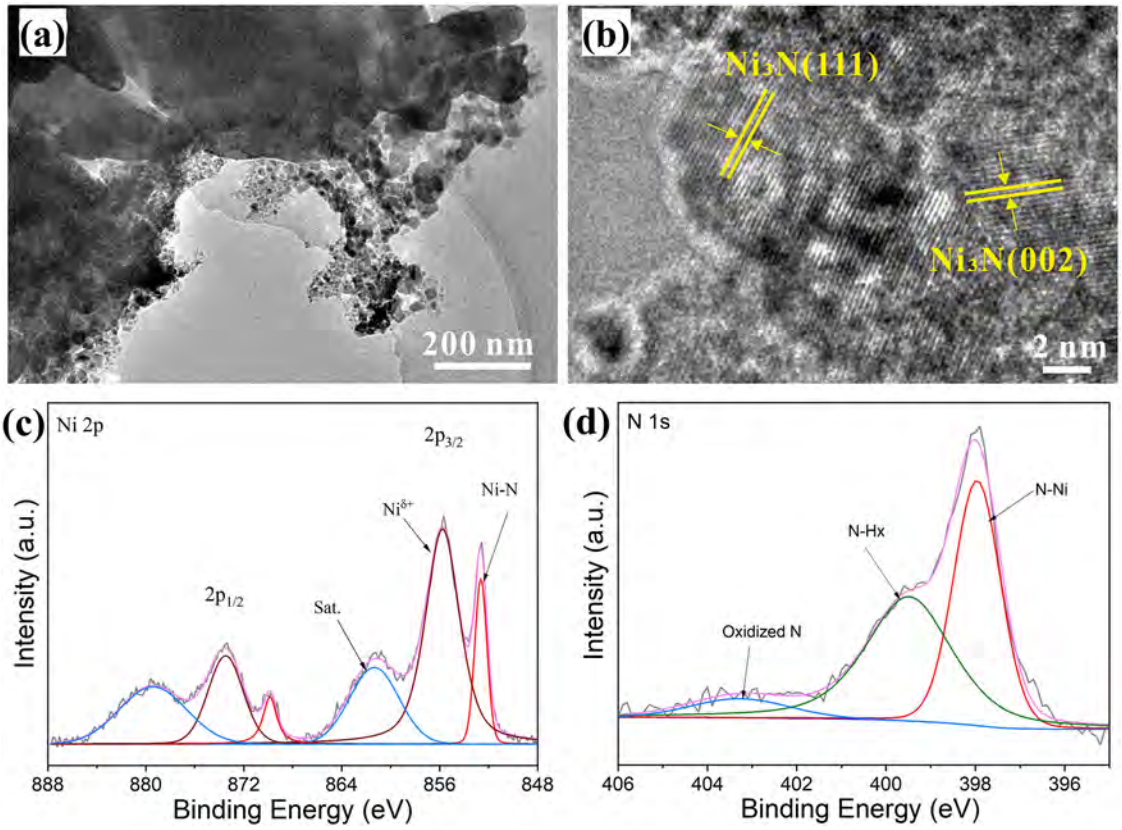

FIG. 2. (a) TEM and (b) HR-TEM images of Ni_3N-400. XPS spectra of (c) Ni 2*p* and (d) N 1*s*.

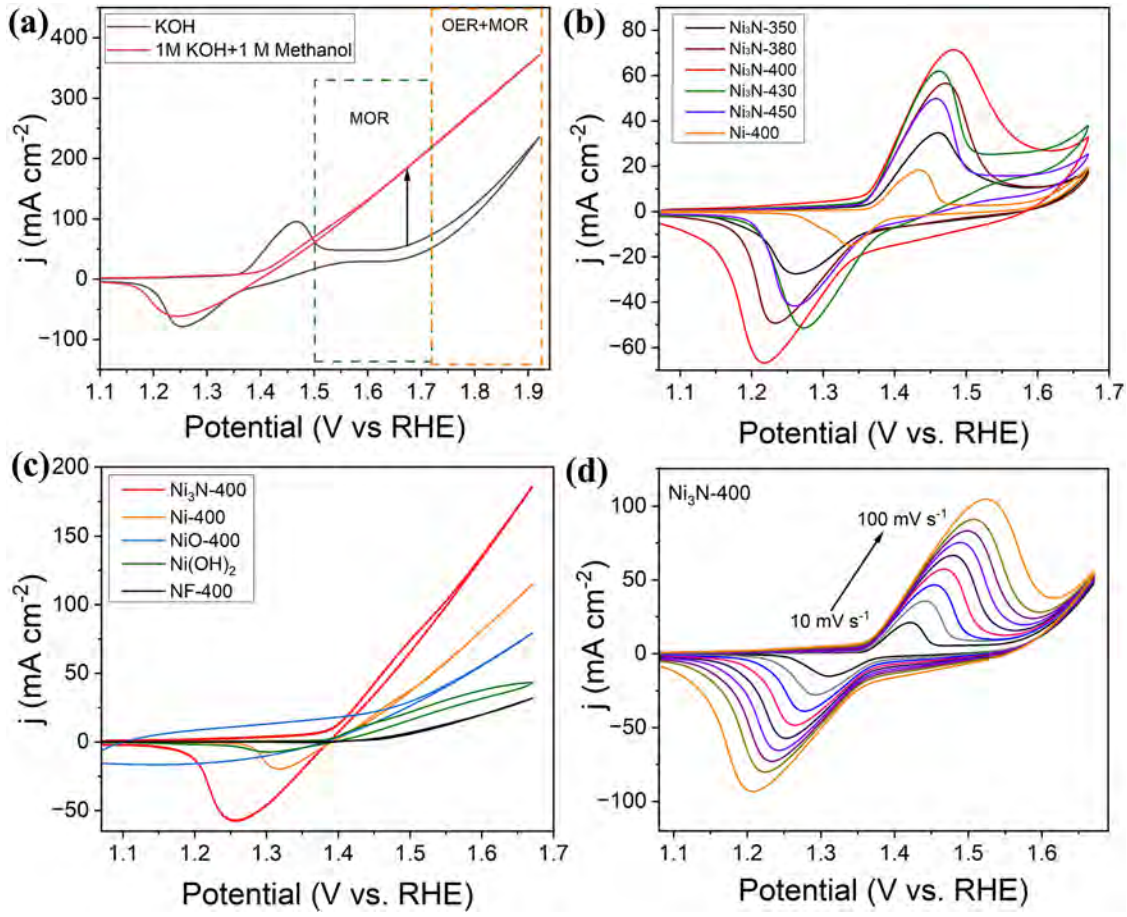

FIG. 3. (a) CV curves of Ni_3N-400 in 1.0M KOH with/without 1.0M methanol solution at the scanning rate of 50 mV s^{-1}. (b) CV curves of Ni_3N at different temperatures and Ni-400 in 1.0M KOH at the scanning rate of 50 mV s^{-1}. (c) CV curves of Ni_3N-400, NF-400, Ni-400, NiO-400, and $Ni(OH)_2$ precursors in 1.0M KOH/1.0M CH_3OH at the scanning rate of 50 mV s^{-1}. (d) CV curves of Ni_3N-400 catalyst at different scanning rates in 1.0M KOH.

whereas OER occurs on the catalyst at about 1.75 V vs RHE with a large overpotential, demonstrating the superior performance of the catalyst at a lower MOR potential compared to OER. Therefore, the potential range for evaluating the MOR activity of Ni_3N-400 is determined to be 1.1–1.7 V.

According to the MOR mechanism of the Ni-based catalysts, the reaction proceeds as follows:[23]

$$Ni + 2OH^- \longrightarrow Ni(OH)_2 + 2e^-, \quad (1)$$

$$Ni(OH)_2 + OH^- \longrightarrow NiOOH + H_2O + e^-, \quad (2)$$

$$NiOOH + CH_3OH \longrightarrow Ni(OH)_2 + \text{products}. \quad (3)$$

As the formation of NiOOH is very imperative to methanol oxidation, all the samples are subjected to CV tests for 50 cycles at 50 mV s^{-1} in 1.0M KOH solution [Fig. 3(b)]. The samples are pretreated to promote the formation of $Ni(OH)_2$/NiOOH on the surface and thicken the electrocatalytic layers.[23,24] As demonstrated in Fig. 3(b), all the catalysts exhibit two redox peaks corresponding to the Ni^{2+}/Ni^{3+} redox reaction. Among them, Ni_3N-400 shows the highest oxidation/reduction peak current density, indicating more exposed active sites on the catalyst in 1.0M KOH solution.[25]

To confirm the better performance of Ni_3N-400, CV is again performed to compare to the control catalysts prepared under a different atmosphere at 400 °C denoted as Ni_3N–Y [NF-400, $Ni(OH)_2$, NiO-400, and Ni-400] [Fig. 3(c), Fig. S2] and under a NH_3 atmosphere at different temperatures Ni_3N–Y (Y = 350, 380, 400, 430, and 450) (Fig. S3) in 1.0M KOH/1.0M CH_3OH. As shown in Fig. 3(c), Ni_3N-400 exhibits the highest current density at 1.6 V, which is 1.6 times that of NF-400, indicating that it has the highest MOR activity among the catalysts. As the MOR response of the Ni_3N-400 catalyst is much faster than the other control catalysts, the surface coverage is estimated by performing CV at different scanning rates (10–100 mV s^{-1}) in 1.0M KOH (Γ^*) [Fig. 3(d)]. As the scanning rates increase from 10 to 100 mV s^{-1}, the current densities increase, the anodic peak at about 1.45 V shifts to larger potentials, and the

cathodic peak at 1.35 V shifts to the lower potentials. The peak potentials show a hysteresis effect due to the sluggish reaction kinetics, as the time is insufficient for the formation of Ni^{3+} at higher scanning speeds.[22] The shift of the anodic and the cathodic peak current densities (I_{pa} and I_{pc}) with the scanning rate (v) for the Ni_3N-400 electrode is depicted in Fig. S4, which clearly shows a linear proportionality between the peak current densities of the Ni^{2+}/Ni^{3+} redox and scanning rate. As a result, the surface coverage of the Ni^{2+}/Ni^{3+} redox species in the Ni_3N-400 electrode can be calculated from the following equation:[1]

$$I_p = (n^2F^2/4RT)\nu A\Gamma^*, \quad (4)$$

where *Ip*, *n*, *R*, *T*, *A*, *v*, and Γ^* are the peak current density, number of transferred electrons, general gas constant, temperature, apparent area of the electrode, potential scanning rate, and surface coverage of the redox species, respectively. The Γ^* value of the Ni_3N-400 is found to be 9.15×10^{-7} mol cm^{-2}, revealing large surface coverage of redox species based on the average of anodic and cathodic results. Notably, the Ni_3N-400 has a larger Γ^*, which is about 1.9, 2.7, 4.4, and 6.5 times larger than those reported in the literature (Table I). The electrochemical activities of the Ni_3N-400 are investigated by the Randles–Sevcik equation,[1]

$$I_p = 2.69 \times 10^4 n^{3/2} A D^{1/2} C v^{1/2}, \quad (5)$$

where *Ip*, *n*, *A*, *D*, *C*, and *v* are the anodic peak current, number of transferred electrons, apparent area of the electrode, proton diffusion coefficient, proton concentration, and potential scanning rate, respectively.

Figure S4c shows the linear relationship between the current density of the anodic peak and the square root of the scanning rate, indicating that Ni^{2+}/Ni^{3+} is a diffusion-controlled process.[28] Therefore, using the above equation, the proton diffusion coefficient (*D*) is used to characterize the oxidation behavior of the electrocatalysts. *D* is estimated to be 10.73×10^{-7} cm^2 s^{-1} for Ni_3N-400. It is important to note that this *D* value is larger than previously reported values (Table I), and moreover, the *D* value of Ni_3N-400 is more than two times higher than those of other samples (Table S1).

To further study the insight into the better MOR characteristics of Ni_3N-400, the electrochemical double layer capacitance (C_{dl}) is employed to estimate the ECSA of the as-prepared samples. C_{dl} is projected by CVs with different scanning rates, as shown in Figs. S5–S10. The high C_{dl} value implies a larger ECSA (Fig. S7) due to enhanced anion exchange ability between the electrolyte and catalytic active sites. As shown in Fig. S7b, the Ni_3N-400 electrode has the largest C_{dl} of 10.84 mF cm^{-2} and a larger ECSA (271 cm^{-2}), which is greater than all the Ni_3N-based catalysts prepared at different temperatures (Table S1). The larger ECSA of Ni_3N-400 signifies that the rational design of the self-supported, uniformly assembled nanosheet arrays can effectively increase the accessibility of active sites.[29]

The kinetics of the samples are investigated by EIS. The diameter of the semi-circle in the Nyquist plot denotes the charge transfer resistance (R_{ct}). Ni_3N-400 exhibits the smallest semi-circle, as shown in Fig. S11, compared to Ni-400 and pristine NF. The small semi-circle relates to the low mass transfer resistance and high electron transfer rate, contributing to the best MOR kinetics. Therefore, it can be concluded that the highly electrocatalytic performance of Ni_3N-400 is not only due to increased ECSA but also the formation of active interface/sites, rapid reaction kinetics, and lower R_{ct} value. To further evaluate the reaction kinetics of the MOR, Tafel slopes are calculated. Generally, a small Tafel slope represents fast electrochemical kinetics that favor the high catalytic activity. As shown in Fig. S12, the Ni_3N-400 catalyst exhibits a Tafel value of 84 mV dec^{-1}, which is significantly lower than that of Ni-400 (94.7 mV dec^{-1}), $Ni(OH)_2$ (113 mV dec^{-1}), NF-400 (126 mV dec^{-1}), and NiO-400 (477 mV dec^{-1}), indicating significantly faster catalytic kinetics.

In order to determine the durability and stability of the anodic catalyst in DMFC, chronoamperometry (CA) is performed in 1.0M KOH/CH_3OH at 0.5 V for 10 000 s (Fig. S13a). The Ni_3N-400 catalyst shows the highest current density among the catalysts even after 10 000 s. To further demonstrate the high stability of Ni_3N-400, the i–t test is continuously repeated for 20 h under the same conditions, while the electrolyte is changed every 5 h [Fig. 4(a)]. After 20 h, the retention rate of Ni_3N-400 is still 72.58%, which is the highest among the other Ni-based catalysts, indicating a greater tolerance for the intermediates formed during methanol oxidation (Table I). However, the 27% decrease in stability may stem from that some of the NiOOH species during MOR are changed to $Ni(OH)_2$ and from the poisoning of the active sites.[24,30] This is further confirmed by the CV results (Fig. S13b) that the peak current densities of the Ni^{2+}/Ni^{3+} redox after the 20-h stability test decrease compared to the initial sample. In addition, the stability of the

TABLE I. Comparison of the MOR properties of Ni_3N NSAs/NF-400 with those of recently reported Ni-based catalysts (j: current density, Γ^*: surface coverage, and D: diffusion coefficient).

Catalyst	j (mA cm^{-2})	Γ^* (10^{-7} mol cm^{-2})	D (10^{-7} cm^2 s^{-1})	Durability (i–t) activity retention	Reference
Ni_3N-400	186.15	9.15	4.73	72.58% after 20 h at 0.6 V (SCE)	This work
NiSn (2:1)	⋯	2.10	1.9×10^{-4}	~96% after 5000 s at 0.7 V (Hg/HgO)	1
$Ni_{0.5}Co_{0.5}Sn$	64.5	1.42	0.128	~76.9% after 1000 s at 0.6 V (Hg/HgO)	3
Ni–C–30	30	0.89	⋯	~85.7% 1800 s at 0.7 V (Hg/HgO)	26
$Ni_{0.75}Cu_{0.25}$	84	4.48	0.289	~91% after 1200 s at 0.65 V (Ag/AgCl)	2
Cu/NiCu	34.6	0.019	⋯	~95% after 10 000 s at 1.55 V (vs RHE)	27
$Ni_{97}Bi_3$	199	3.9	2.0	78% after 12 h at 0.55 V (Ag/AgCl)	25

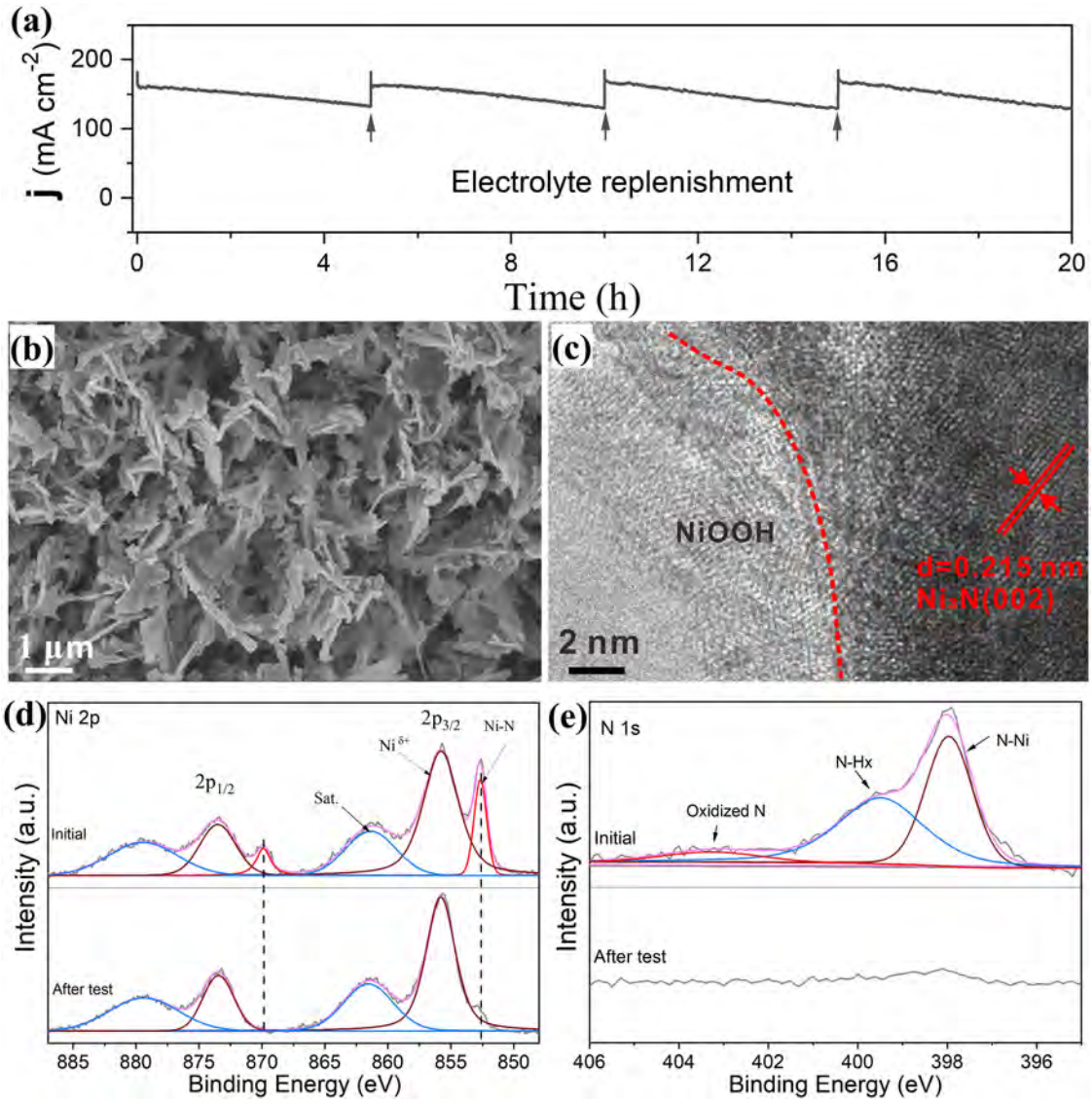

FIG. 4. (a) The i–t curve of the Ni_3N-400 catalyst with electrolyte replacement every 5 h at 0.6 V in the 1.0M KOH/CH_3OH solution. (b) SEM and (c) HR-TEM images, and [(d) and (e)] XPS of Ni_3N NSAs/NF-400 after the i–t test for 20 h.

catalyst is studied by continuous CV scanning. As shown in Fig. S13c, the retention rate of all the samples is 70%, while Ni_3N-400 shows a 74.25% retention rate after 1000 cycles. The SEM and TEM images shown in Fig. 4(b) and 4(c) demonstrate that electrocatalysis has no discernible effects on the size and morphology of Ni_3N-400 and that no growth or agglomeration occurs. XRD also shows no changes in the catalyst crystallinity, confirming the outstanding durability of Ni_3N-400 during MOR (Fig. S14). It is noted that an amorphous layer of about 3 nm is formed at the edges site after the long-time test [Fig. 4(c)]. This layer is composed of NiOOH active species,[31,32] and XPS confirms that the NiOOH species are formed on the surface of the sample. Comparing the Ni 2*p* spectra of Ni_3N-400, the Ni–N peak at 852.7 eV vanishes. In addition, all the peaks of Ni_3N-400 in the N 1*s* spectrum disappear due to the absence of Ni_3N as it reacts to form new active species of NiOOH.[31] These results suggest that Ni_3N-400 has a good long-term stability as an anode electrocatalyst in DMFCs due to the excellent structural stability of the mesoporous Ni_3N and surface-active species NiOOH.

CONCLUSION

A self-supporting catalyst composed of hierarchical Ni_3N NSAs on Ni foam is demonstrated for enhanced MOR via ammonification.

The Ni_3N catalyst delivers the best MOR performance in alkaline media as manifested by a current density of 186.15 mA cm^{-2} and high durability of up to 20 h at a retention rate of 72.58%. The good characteristics are attributed to the following reasons: (1) the highly porous nanosheet arrays comprised of small nanoparticles expose more active sites and facilitate fast charge/mass transfer; (2) Ni foam acts as a conductive support to provide abundant catalytic active sites by dispersing the active centers, resulting in a high loading of Ni_3N NSAs; and (3) the stability is significantly improved due to the seamless contact between Ni_3N nanosheet arrays and Ni foam, thus preventing leaching and triggering rapid charge transfer and producing synergistic effects between Ni_3N NSAs and Ni foam. The findings reveal a significant step forward in the development of highly efficient and economically viable electrocatalysts in the pursuit of efficient DMFCs.

SUPPLEMENTARY MATERIAL

See the supplementary material for Figures S1–S14 and Table S1.

ACKNOWLEDGMENTS

This work was financially supported by the 2022 Special Fund Project for Science and Technology Innovation Strategy of Guangdong Province (Grant Nos. STKJ202209083 and STKJ202209077), the 2020 Li Ka Shing Foundation Cross-Disciplinary Research Grant (Grant Nos. 2020LKSFG01A and 2020LKSFG09A), Jieyang Science and Technology Project (Grant No. skjcx039), City University of Hong Kong Strategic Research Grant (SRG) (Grant No. 7005505), and City University of Hong Kong Donation Research Grant (Grant No. DON-RMG No. 9229021).

AUTHOR DECLARATIONS

Conflict of Interest

The authors have no conflicts to disclose.

Author Contributions

Wanying Zhang and Madiha Rafiq contributed equally to this work.

Wanying Zhang: Conceptualization (equal). **Madiha Rafiq**: Writing – original draft (equal). **Jingcheng Lu**: Validation (supporting). **Abebe Reda Woldu**: Writing – review & editing (supporting). **Jianhong Zhou**: Formal analysis (supporting). **Hong Xia**: Methodology (supporting). **Paul K. Chu**: Writing – review & editing (equal). **Liangsheng Hu**: Project administration (equal); Resources (equal); Supervision (equal); Writing – review & editing (equal). **Fushen Lu**: Project administration (equal); Resources (equal); Supervision (equal).

DATA AVAILABILITY

The data supporting the results of this study are available upon reasonable request from the corresponding author.

REFERENCES

[1] J. Li, Z. Luo, Y. Zuo, J. Liu, T. Zhang, P. Tang, J. Arbiol, J. Llorca, and A. Cabot, Appl. Catal., B **234**, 10 (2018).
[2] X. Cui, P. Xiao, J. Wang, M. Zhou, W. Guo, Y. Yang, Y. He, Z. Wang, Y. Yang, Y. Zhang, and Z. Lin, Angew. Chem., Int. Ed. **56**(16), 4488 (2017); J. Li, Y. Zuo, J. Liu, X. Wang, X. Yu, R. Du, T. Zhang, M. F. Infante-Carrió, P. Tang, J. Arbiol, J. Llorca, Z. Luo, and A. Cabot, J. Mater. Chem. A **7** (38), 22036 (2019); Y. Yu, Q. Yang, X. Li, M. Guo, and J. Hu, Green Chem. **18** (9), 2827 (2016).
[3] J. Li, Z. Luo, F. He, Y. Zuo, C. Zhang, J. Liu, X. Yu, R. Du, T. Zhang, M. F. Infante-Carrió, P. Tang, J. Arbiol, J. Llorca, and A. Cabot, J. Mater. Chem. A **6**(45), 22915 (2018).
[4] M. Mazloum-Ardakani, V. Eslami, and A. Khoshroo, Mater. Sci. Eng., B **229**, 201 (2018); X. Zhao, M. Yin, M. Liang, L. Liang, C. Liu, J. Liao, T. Lu, and W. Xing, Energy Environ. Sci. **4**(8), 2736 (2011); H. Huang and X. Wang, J. Mater. Chem. A **2**(18), 6266 (2014); S. Sharma and B. G. Pollet, J. Power Sources **208**, 96 (2012); S. L. Madaswamy, A. A. Alothman, M. M. Al-Anazy, A. A. Ifseisi, K. N. Alqahtani, S. K. Natarajan, S. Angaiah, and D. Ragupathy, J. Ind. Eng. Chem. **97**, 79 (2021).
[5] D. Wei, L. Ma, M. Gan, S. Han, J. Shen, J. Ding, W. Zhan, C. Zhou, X. Zhong, and F. Xie, Int. J. Hydrogen Energy **45**(7), 4875 (2020).
[6] J.-T. Liu, L.-S. Hu, Y.-L. Liu *et al.*, "Real-time monitoring of auxin vesicular exocytotic efflux from single plant protoplasts by amperometry at microelectrodes decorated with nanowires," Angew. Chem. Int. Ed. **53**(10), 2643–2647 (2014).
[7] J. T. Zhang, A. R. Woldu, X. Zhao *et al.*, "Plasmon-enhanced hydrogen evolution on Pt-anchored titanium nitride nanowire arrays," Appl. Surf. Sci. **598**, 153745 (2022).
[8] J. Zhu, L. S. Hu, P. X. Zhao *et al.*, "Recent advances in electrocatalytic hydrogen evolution using nanoparticles," Chem. Rev. **120**(2), 851–918 (2020).
[9] J. W. Zhang, Y. L. Yuan, L. Gao *et al.*, "Stabilizing Pt-based electrocatalysts for oxygen reduction reaction: Fundamental understanding and design strategies," Adv. Mater. **33**(20), 2006494 (2021).
[10] A. Serov and C. Kwak, Appl. Catal., B **90**(3), 313 (2009); Q. Q. Chen, C. C. Du, Y. X. Yang, Q. H. Shen, J. F. Qin, M. Hong, X. H. Zhang, and J. H. Chen, Mater. Today Phys. **30**, 100931 (2023); T. Xia, K. Zhao, Y. Zhu, X. Bai, H. Gao, Z. Wang, Y. Gong, M. Feng, S. Li, Q. Zheng, S. Wang, R. Wang, and H. Guo, Adv. Mater. **35** (2), 2206508 (2023).
[11] M. V. Martínez-Huerta, S. Rojas, J. L. Gómez de la Fuente, P. Terreros, M. A. Peña, and J. L. G. Fierro, Appl. Catal., B **69**(1), 75 (2006); Y. Tong, X. Yan, J. Liang, and S. X. Dou, Small **17**(9), 1904126 (2021); N. Wu, M. Zhai, F. Chen, X. Zhang, R. Guo, T. Hu, and M. Ma, Nanoscale **12**(42), 21687 (2020); C. J. Weiss, P. Das, D. L. Miller,M. L. Helm, and A. M. Appel, ACS Catal. **4**(9), 2951 (2014).
[12] F. Song, W. Li, J. Yang, G. Han, P. Liao, and Y. Sun, Nat. Commun. **9**(1), 4531 (2018).
[13] W. Ni, A. Krammer, C. S. Hsu, H. M. Chen, A. Schüler, and X. Hu, Angew. Chem., Int. Ed. **58**(22), 7445 (2019); B. Liu, B. He, H.-Q. Peng, Y. Zhao, J. Cheng, J. Xia, J. Shen, T.-W. Ng, X. Meng, C.-S. Lee, and W. Zhang, Adv. Sci. **5**(8), 1800406 (2018).
[14] W.-F. Chen, K. Sasaki, C. Ma, A. I. Frenkel, N. Marinkovic, J. T. Muckerman, Y. Zhu, and R. R. Adzic, Angew. Chem., Int. Ed. **51**(25), 6131 (2012).
[15] M. Gong, D.-Y. Wang, C.-C. Chen, B.-J. Hwang, and H. Dai, Nano Res. **9**(1), 28 (2016); F. Safizadeh, E. Ghali, and G. Houlachi, Int. J. Hydrogen Energy **40**(1), 256 (2015).
[16] T. Kou, T. Smart, B. Yao, I. Chen, D. Thota, Y. Ping, and Y. Li, Adv. Energy Mater. **8**(19), 1703538 (2018); R.-Q. Li, Q. Liu, Y. Zhou, M. Lu, J. Hou, K. Qu, Y. Zhu, and O. Fontaine, J. Mater. Chem. A **9**(7), 4159 (2021); B. Wang, S. Jiao, Z. Wang, M. Lu, D. Chen, Y. Kang, G. Pang, and S. Feng, J. Mater. Chem. A **8**(33), 17202 (2020).
[17] S. Hu, C. Feng, S. Wang, J. Liu, H. Wu, L. Zhang, and J. Zhang, ACS Appl. Mater. Interfaces **11**(14), 13168 (2019).
[18] D. Gao, J. Zhang, T. Wang, W. Xiao, K. Tao, D. Xue, and J. Ding, J. Mater. Chem. A **4**(44), 17363 (2016).
[19] M. Jiang, Y. Li, Z. Lu, X. Sun, and X. Duan, Inorg. Chem. Front. **3**(5), 630 (2016).
[20] L. Yu, S. Song, B. McElhenny, F. Ding, D. Luo, Y. Yu, S. Chen, and Z. Ren, J. Mater. Chem. A **7**(34), 19728 (2019).
[21] B. Zhang, C. Xiao, S. Xie, J. Liang, X. Chen, and Y. Tang, Chem. Mater. **28**(19), 6934 (2016).

[22]D. Chen and S. D. Minteer, J. Power Sources **284**, 27 (2015).
[23]J. Wang, D. Teschner, Y. Yao, X. Huang, M. Willinger, L. Shao, and R. Schlögl, J. Mater. Chem. A **5**(20), 9946 (2017).
[24]H. Sun, Y. Ye, J. Liu, Z. Tian, Y. Cai, P. Li, and C. Liang, Chem. Commun. **54**(13), 1563 (2018).
[25]A. A. Dubale, Y. Zheng, H. Wang, R. Hübner, Y. Li, J. Yang, J. Zhang, N. K. Sethi, L. He, Z. Zheng, and W. Liu, Angew. Chem., Int. Ed. **59**(33), 13891 (2020).
[26]R. M. Abdel Hameed and R. M. El-Sherif, Appl. Catal., B **162**, 217 (2015).
[27]D. Wu, W. Zhang, and D. Cheng, ACS Appl. Mater. Interfaces **9**(23), 19843 (2017).
[28]X. Cui, Y. Yang, Y. Li, F. Liu, H. Peng, Y. Zhang, and P. Xiao, J. Electrochem. Soc. **162**(14), F1415 (2015); S.-J. Zhang, Y.-X. Zheng, L.-S. Yuan, and L.-H. Zhao, J. Power Sources **247**, 428 (2014).
[29]H. Huang, C. Yu, X. Han, S. Li, S. Cui, C. Zhao, H. Huang, and J. Qiu, Ind. Eng. Chem. Res. **56**(48), 14245 (2017).
[30]X. Wang, S. Xi, W. S. V. Lee, P. Huang, P. Cui, L. Zhao, W. Hao, X. Zhao, Z. Wang, H. Wu, H. Wang, C. Diao, A. Borgna, Y. Du, Z. G. Yu, S. Pennycook, and J. Xue, Nat. Commun. **11**(1), 4647 (2020).
[31]Y. Li, L. Hu, W. Zheng, X. Peng, M. Liu, P. K. Chu, and L. Y. S. Lee, Nano Energy **52**, 360 (2018).
[32]A. Qayum, X. Peng, J. Yuan, Y. Qu, J. Zhou, Z. Huang, H. Xia, Z. Liu, D. Q. Tan, P. K. Chu, F. Lu, and L. Hu, ACS Appl. Mater. Interfaces **14**(24), 27842 (2022).

Supporting Information

Durable Ni_3N porous nanosheets array for non-noble metal methanol oxidation reaction

Wanying Zhang[a,1], Madiha Rafiq[a,1], Jingcheng Lu[a], Abebe Reda Woldu[a], Jianhong Zhou[a], Hong Xia[a,b], Paul K. Chu[c,], Liangsheng Hu[a,b,*] and Fushen Lu[a,b,*]*

[a] Department of Chemistry and Key Laboratory for Preparation and Application of Ordered Structural Materials of Guangdong Province, Shantou University, Shantou, Guangdong, 515063, P. R. China

[b] Chemistry and Chemical Engineering Guangdong Laboratory, Shantou, 515063, P. R. China

[c] Department of Physics, Department of Materials Science and Engineering, and Department of Biomedical Engineering, City University of Hong Kong, Tat Chee Avenue, Kowloon, Hong Kong, China

[1] Those authors contributed equally to this work

Corresponding Authors: E-mail: paul.chu@cityu.edu.hk (PKC); fslu@stu.edu.cn (FSL); lshu@stu.edu.cn (LSH)

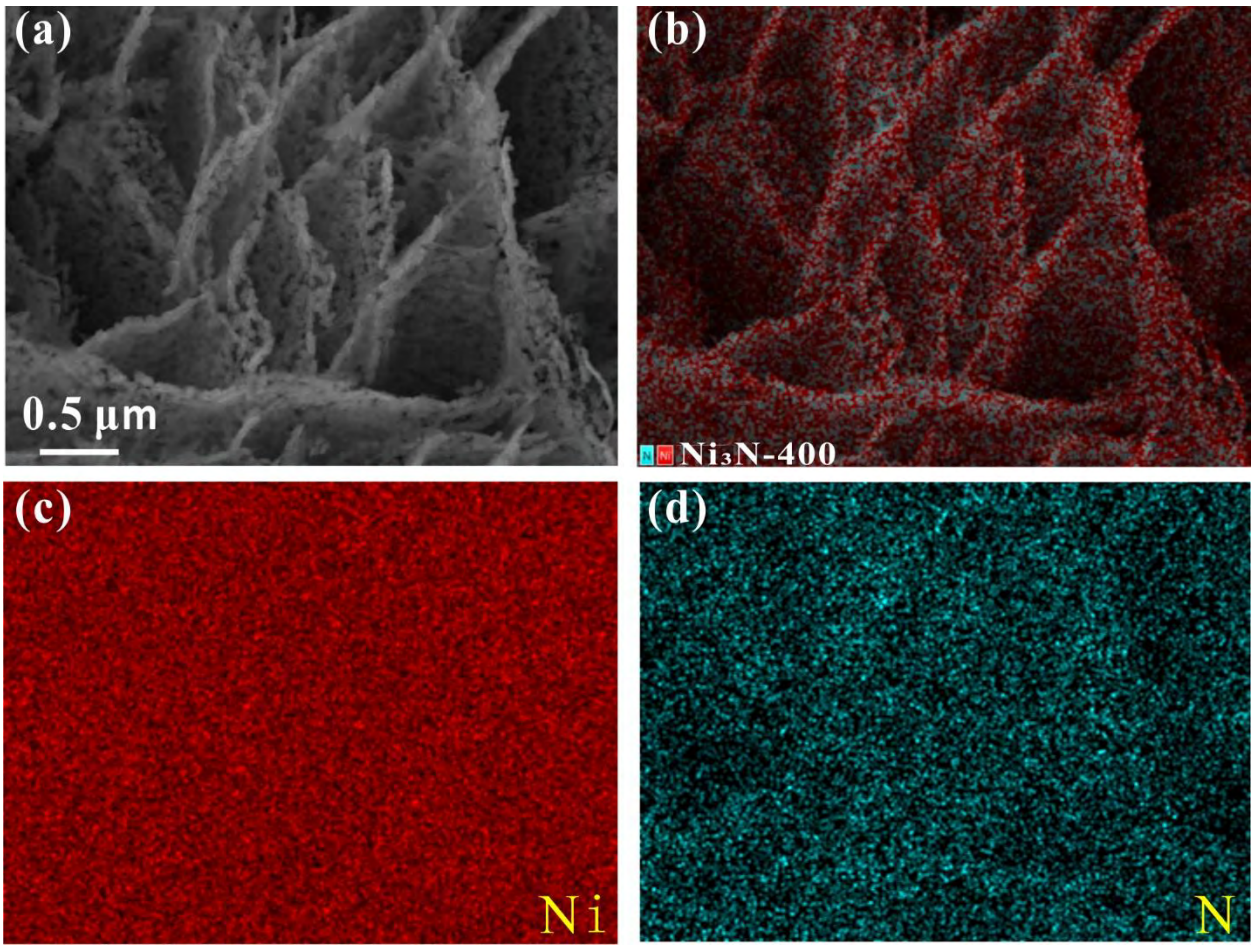

Figure S1. (a) SEM image and (b-d) EDS maps of Ni_3N-400.

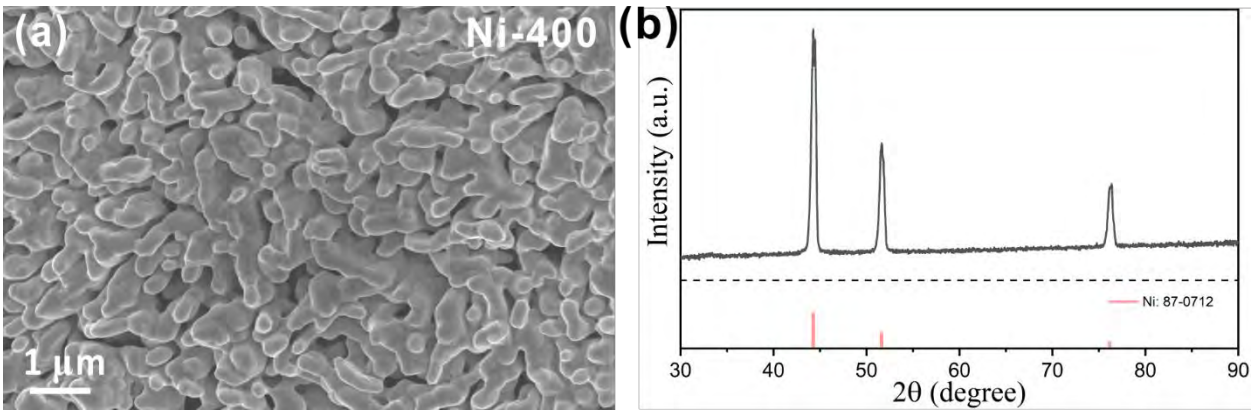

Figure S2. (a) SEM image and (b) XRD pattern of Ni-400 ($Ni(OH)_2$ precursor treated under H_2/Ar).

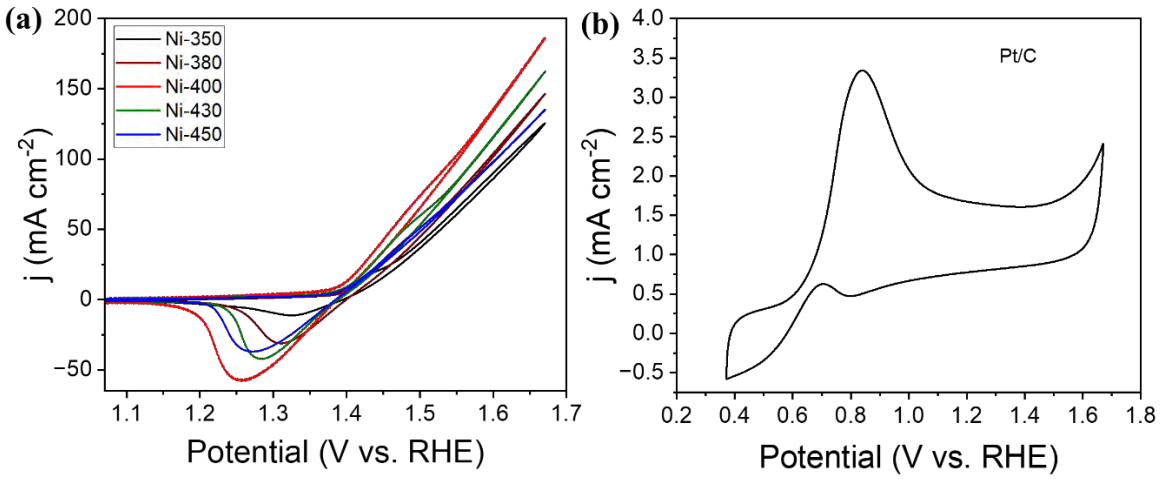

Figure S3. (a) CV curves of Ni_3N-Y in 1.0 M KOH/1.0 M methanol at a scanning rate of 50 mV s^{-1}. (b) CV curve of commercial Pt/C in 1.0 M KOH/1.0 M methanol at a scanning rate of 50 mV s^{-1}.

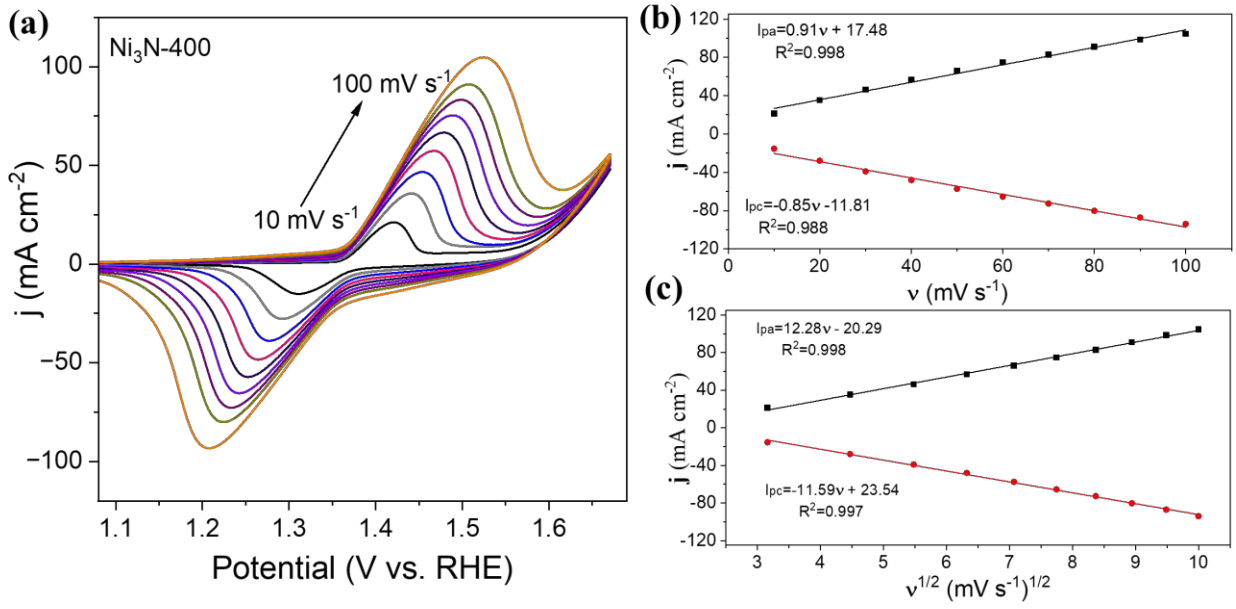

Figure S4. (a) CV curves of Ni_3N-400 at different scanning rates in 1.0 M KOH; (b) Relationship between the peak current densities of the anode and cathode and sweeping rates; (c) Relationship between the peak current densities of the anode and cathode and square root of the scanning rates.

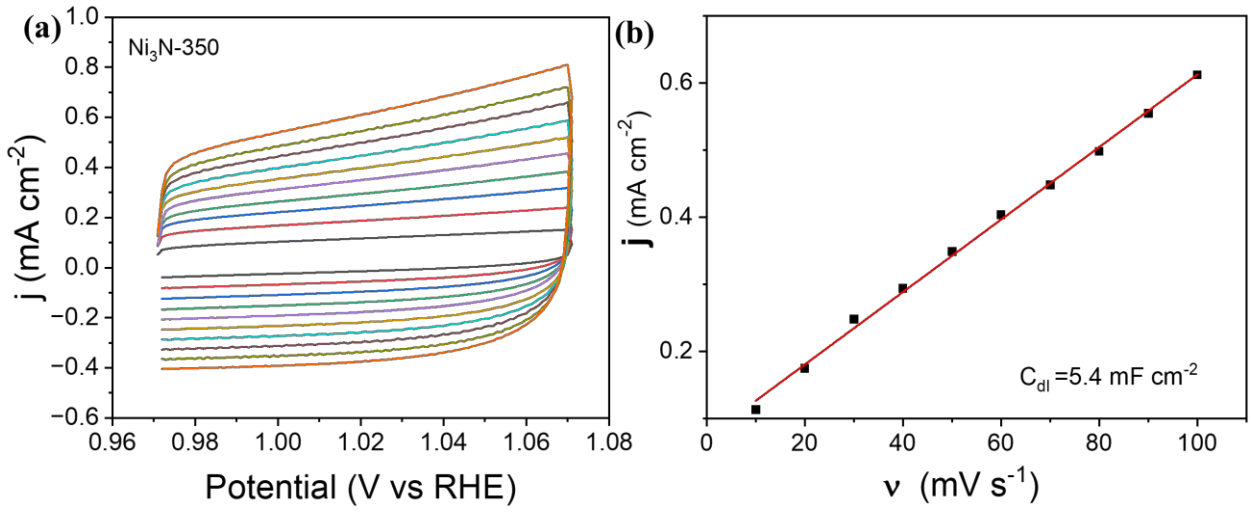

Figure S5. (a) CV curves of Ni_3N-350 at different scanning rates in 1.0 M KOH and (b) Relationship between the capacitance currents and rates for the estimation of C_{dl}.

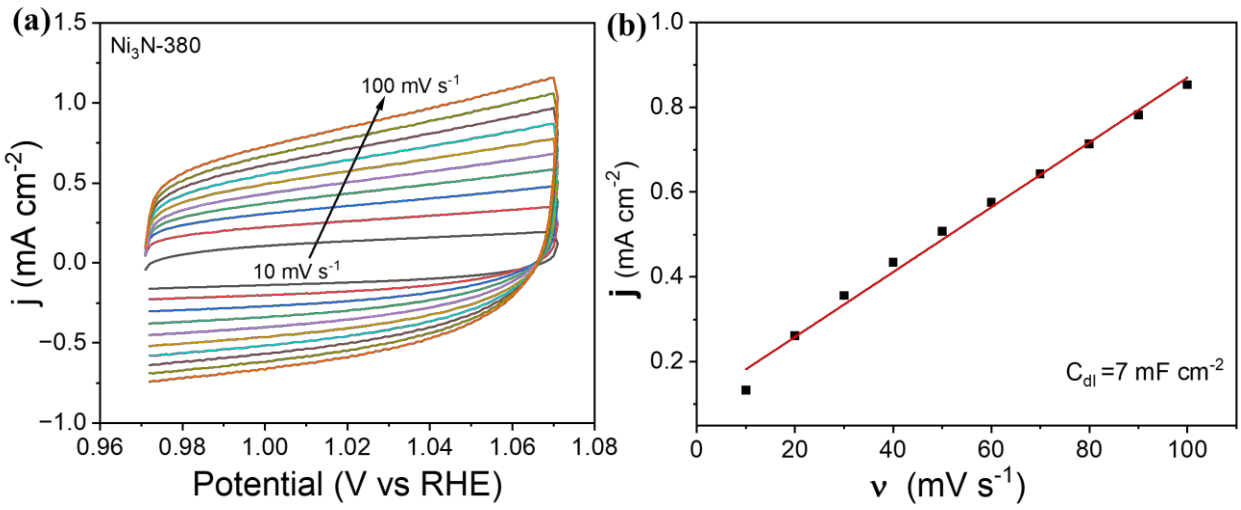

Figure S6. (a) CV curves of Ni_3N-380 at different scanning rates in 1.0 M KOH and (b) Relationship between the capacitance currents and rates for the estimation of C_{dl}.

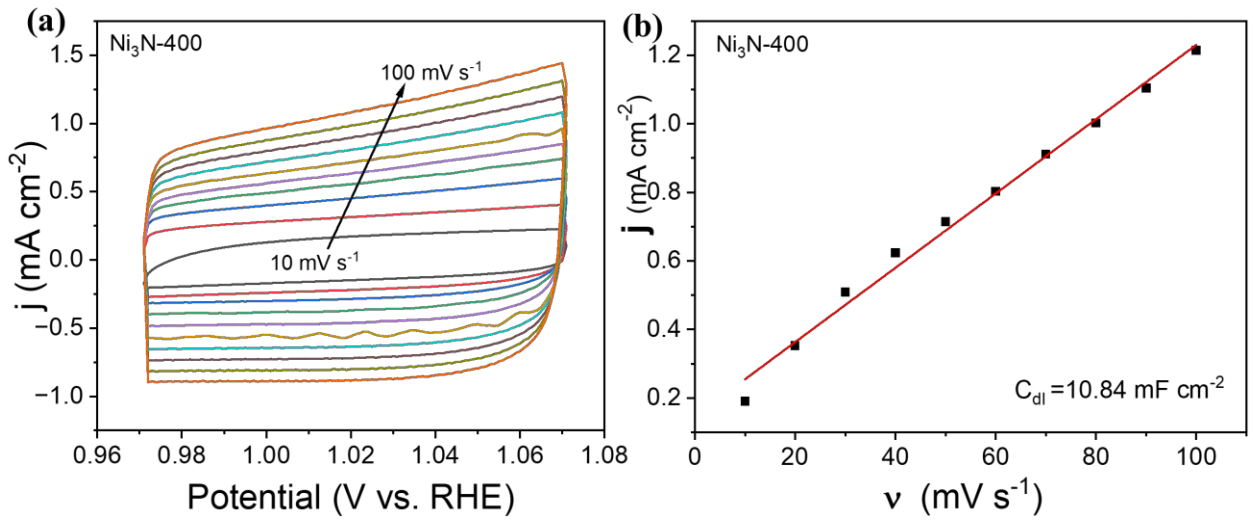

Figure S7. (a) CV curves of Ni_3N-400 at different scanning rates in 1.0 M KOH and (b) Relationship between the capacitance currents and rates for the estimation of C_{dl}.

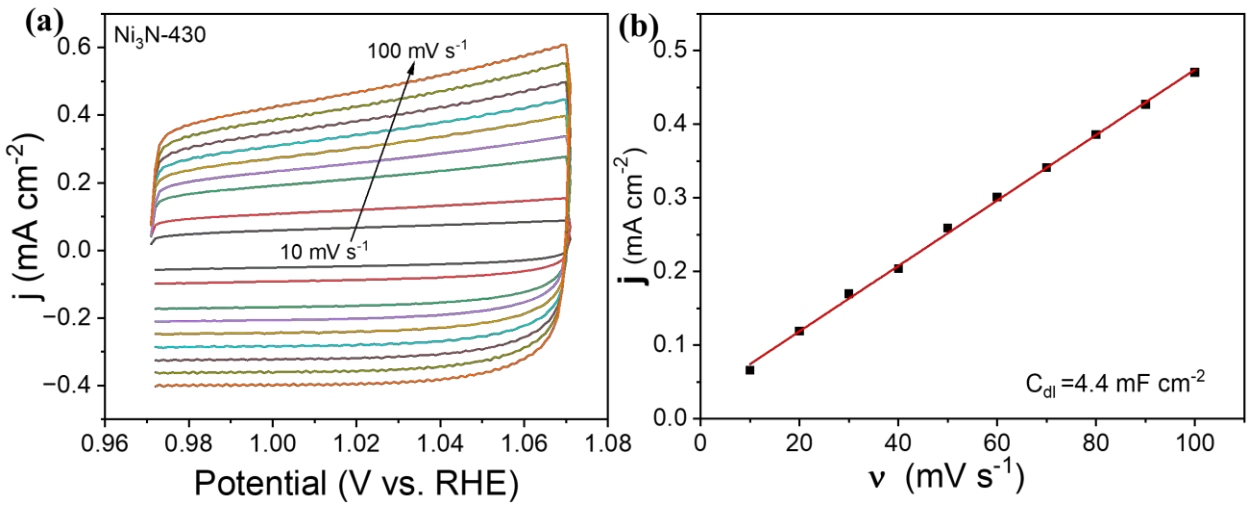

Figure S8. (a) CV curves of Ni_3N-430 at different scanning rates in 1.0 M KOH and (b) Relationship between the capacitance currents and rates for the estimation of C_{dl}.

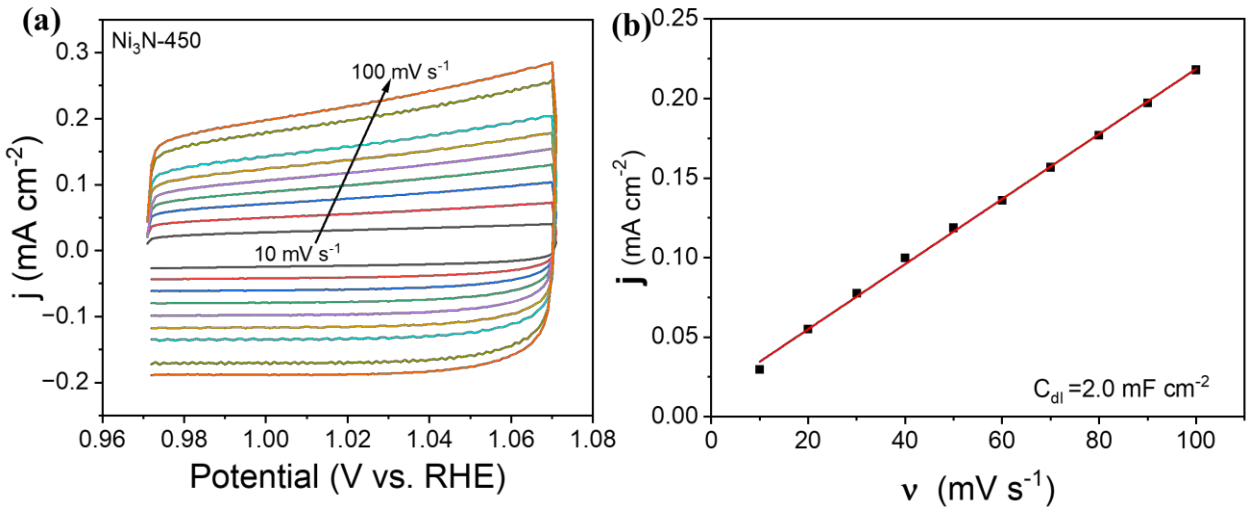

Figure S9. (a) CV curves of Ni_3N-450 at different scanning rates in 1.0 M KOH and (b) Relationship between the capacitance currents and rates for the estimation of C_{dl}.

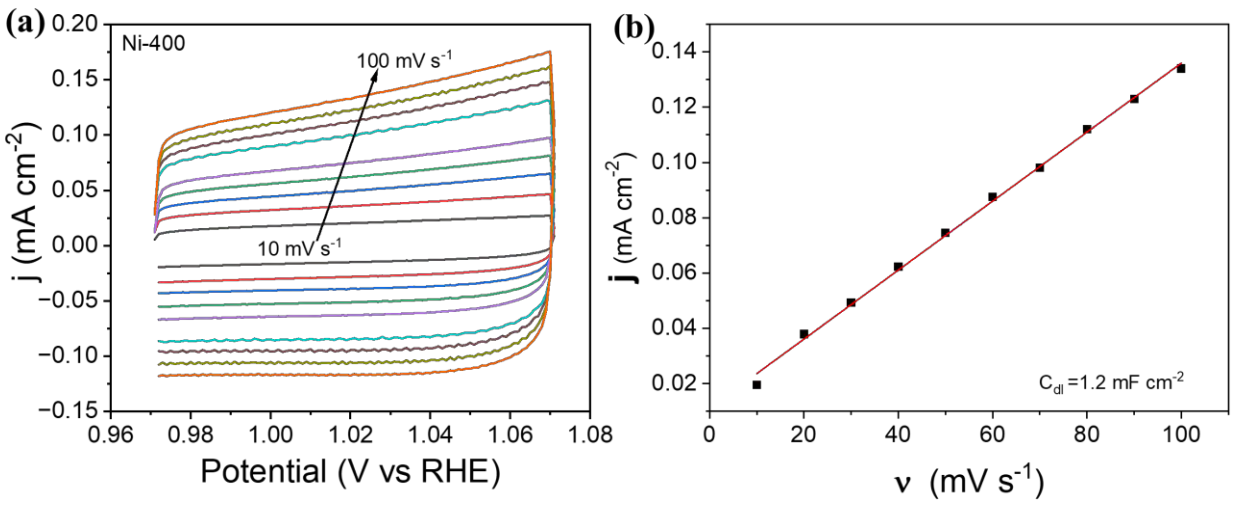

Figure S10. (a) CV curves of Ni-400 at different scanning rates in 1.0 M KOH and (b) Relationship between the capacitance currents and rates for the estimation of C_{dl}.

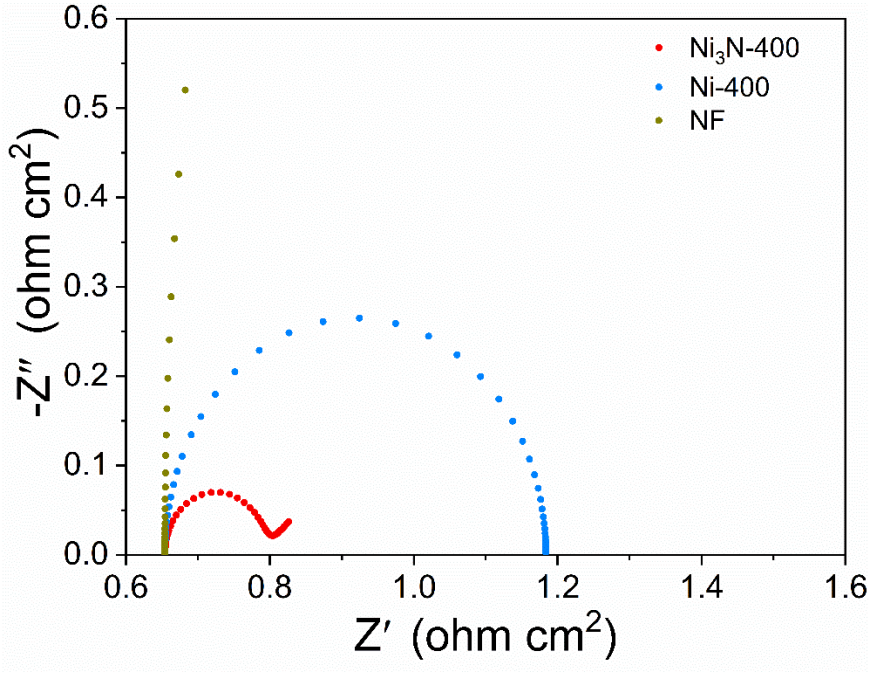

Figure S11. Electrochemical impedance diagrams of Ni_3N-400, Ni-400, and NF-400 at 0.5 V in 1.0 M KOH / 1.0 M methanol.

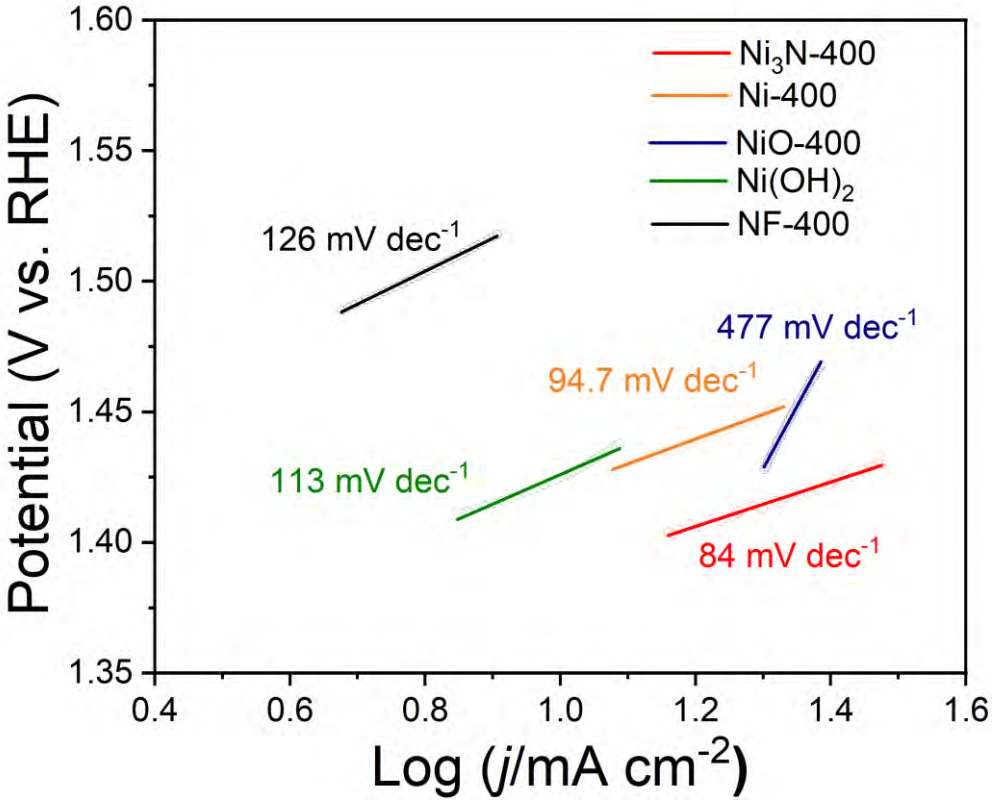

Figure S12. Tafel plots of the Ni_3N-based electrocatalysts.

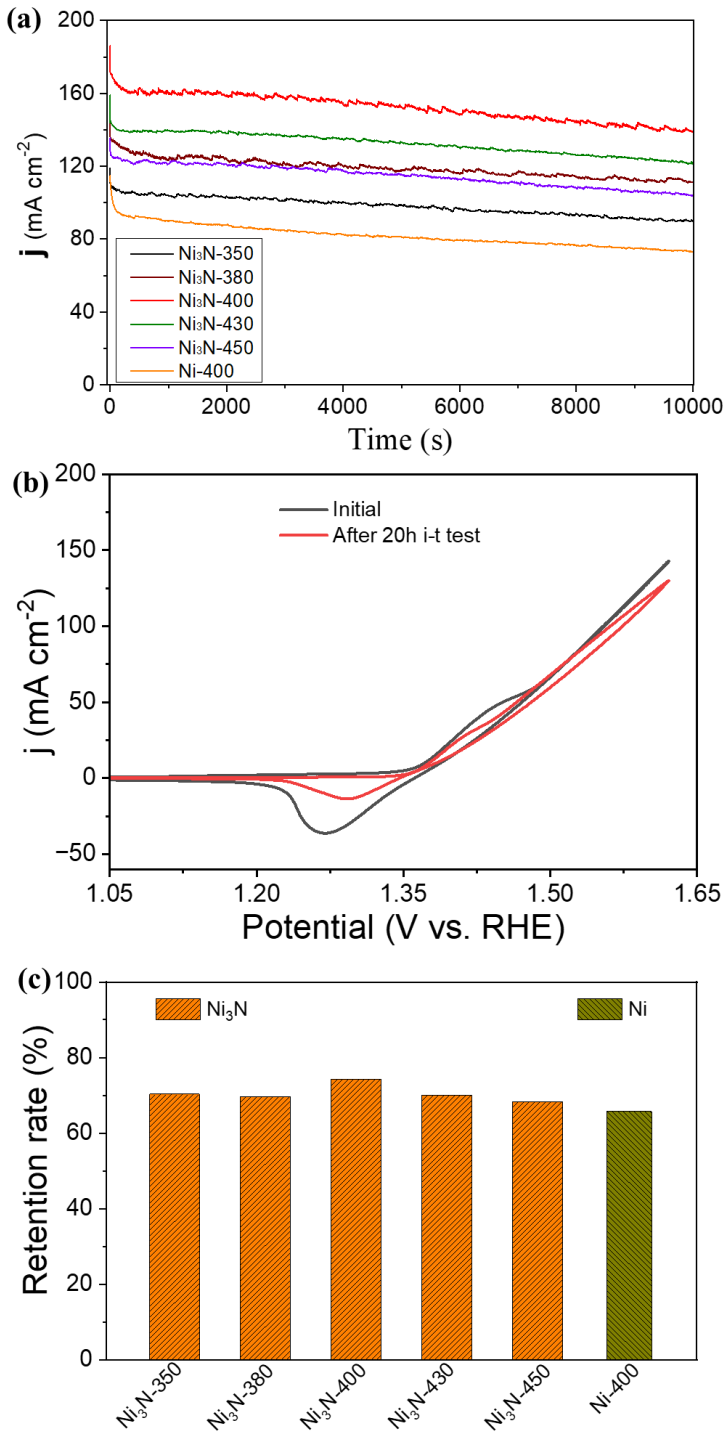

Figure S13. (a) i-t curves of Ni_3N-Y and Ni-400 at 0.6 V; (b) CV curves of Ni_3N-400 before and after 20 h in 1.0 M KOH/1.0 M methanol solution at a scanning rate of 50 mV s^{-1}; (c) Current density retention of Ni_3N-Y and Ni-400 after 1,000 CV cycles.

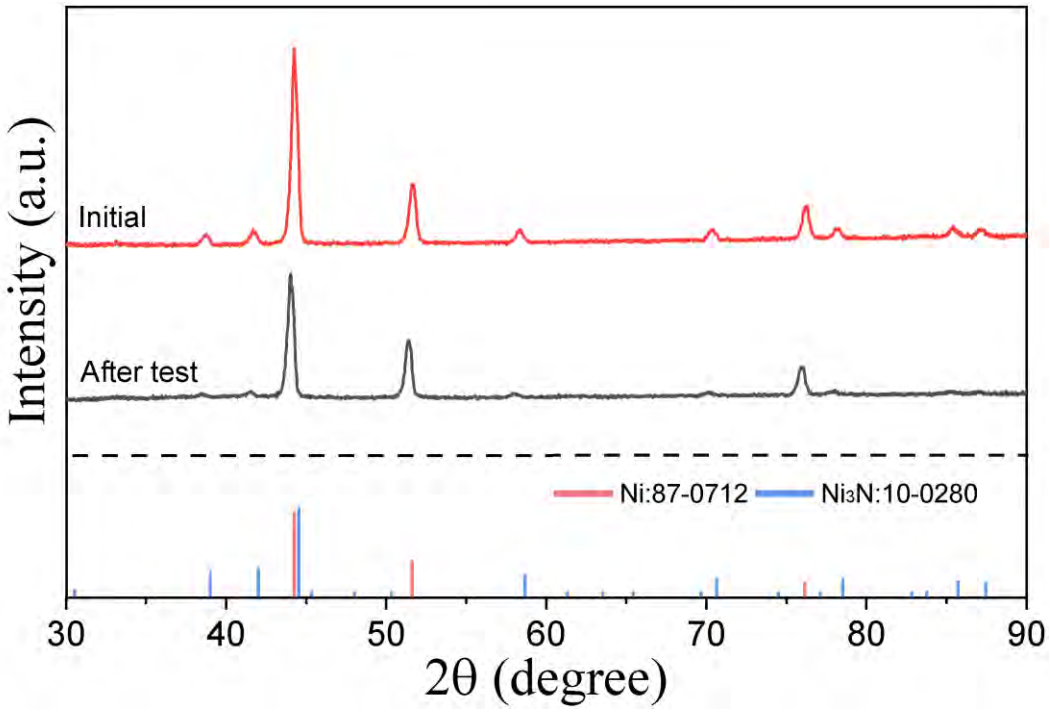

Figure S14. XRD patterns of Ni_3N NSAs/NF-400 before and after the i-t test for 20 h.

Table S1. Electrochemical parameters of the catalysts.

Catalyst	Current density **j** (mA cm^{-2})	Surface coverage Γ*(**10^{-7}** mol cm^{-2}**)**	Diffusion coefficient D(10^{-7} cm^2 s^{-1})	ECSA (cm^2)
Ni3N-350	125.12	6.12	4.73	135
Ni3N-380	146.36	8.08	8.40	175
Ni3N-400	186.15	9.15	10.73	271
Ni3N-430	162.23	8.56	9.29	110
Ni3N-450	135.04	8.07	8.22	50
Ni/NF	115.25	3.73	1.75	30

The electrochemically active surface area (ECSA) of non-noble Ni-based electrocatalysts is generally estimated using the electrochemical double-layer capacitance (C_{dl}) based on the CV curves acquired at different scanning rates in the non-Faradaic potential range. In this potential region, the charge transfer reactions are considered to be negligible and the current originates solely from electrical double-layer charging and discharging. A non-Faradaic potential range is first identified by CV in the quiescent solution. This non-Faradaic region is typically a 0.1 V window centered at the open-circuit potential. All the measured currents in this region are assumed to stem from double-layer charging. Based on this assumption, the charging current, i_c, is equal to the product of electrochemical double layer capacitance C_{dl}, and scanning rate ν, as shown by Eq. (1). [1]

$$i_c = \nu C_{dl}. \qquad (1)$$

Plotting i_c as a function of ν yields a straight line with a slope equal to C_{dl}. The electrochemical double-layer capacitance is measured from the scanning-rate-dependent CVs for Ni_3N-Y. The electrochemically active surface area (ECSA) of the catalyst can be calculated by dividing C_{dl} by

the specific capacitance of the sample as shown by Eq. (2). Here, a general specific capacitance of 0.04 mF cm^{-2} based on typical values reported for metal electrodes in aqueous NaOH solution is used:[1]

$$ECSA = C_{dl}/Cs. \qquad (2)$$

Reference

[1] Cui X, Xiao P, Wang J, et al. Highly branched metal alloy networks with superior activities for the methanol oxidation reaction[J]. Angewandte Chemie International Edition, 2017, 56(16): 4488-4493.